Orthorhombic symmetry and anisotropic properties of β-PbO_2

Piotr Fabrykiewicz,* Radosław Przeniosło,† Nevill Gonzalez Szwacki, and Izabela Sosnowska
Faculty of Physics, University of Warsaw, Pasteura 5, 02-093 Warsaw, Poland

Emmanuelle Suard
Institut Laue Langevin, 71 avenue des Martyrs, 38042 Grenoble, France

François Fauth
ALBA-CELLS, BP1413, 08290 Cerdanyola del Vallés, Barcelona, Spain

(Received 4 November 2020; accepted 12 February 2021; published 26 February 2021)

The structural and electronic properties of the rutile-type oxide β-PbO_2 (plattnerite) are studied by neutron and synchrotron radiation diffraction and first-principles density functional theory (DFT) calculations. Both diffraction measurements and DFT calculations show that β-PbO_2 has a $CaCl_2$-type orthorhombic structure (space group $Pnnm$) instead of the widely accepted β-PbO_2 rutile-type tetragonal structure (space group $P4_2/mnm$). This symmetry lowering in β-PbO_2 is a robust effect observed at ambient pressure at temperatures between 100 and 400 K. The orthorhombic symmetry rules out the possibility of a semimetallic symmetry-protected state in β-PbO_2. Both diffraction measurements and DFT calculations show an anisotropy of thermal expansion, atomic vibrations, and elastic constants of β-PbO_2 along the [100] and [010] directions.

DOI: 10.1103/PhysRevB.103.064109

I. INTRODUCTION

β-PbO_2 has attracted considerable interest because of its fundamental electronic properties as well as its most widespread technical application, i.e., lead-acid battery electrodes that have been in use for the last 160 years [1]. The motivation to study the electronic properties of β-PbO_2 gained some additional impact related to the possible existence of topologically nontrivial [2,3] semimetallic states, as shown recently in [4–6]. Quantitative studies of the physical properties of β-PbO_2 suffer from the lack of possibilities to synthesize single crystals. To the best of our knowledge, there are a few single-crystal studies, e.g., structure determination by x-ray diffraction done using geological β-PbO_2 specimens [7] and x-ray compression studies of β-PbO_2 single crystals [8]. There are many reports of lead oxide films, mainly in electrochemical contexts, but these films (e.g., [9]) are usually composed of a mixture of two phases: β-PbO_2 and α-PbO_2 [10], so most experimental studies have to rely on the available polycrystalline, at best single-phase, β-PbO_2 samples.

The crystal structure of β-PbO_2 (mineral name: plattnerite) is widely assigned to the rutile type [11] with the tetragonal space group $P4_2/mnm$. Studies of β-PbO_2 at ambient conditions (e.g., [7,10–22]) used the tetragonal rutile-type structure. The electronic properties of β-PbO_2 reported in the literature vary from insulating (e.g. [16]) to semimetallic (e.g., [23,24]). The considerable variation of electronic properties of β-PbO_2 is attributed to many factors, including stoichiometry, vacancies, microstructure [25,26], and possible hydrogen content [18]. All these factors make quantitative interpretations of experimental studies difficult. Using the approach of density functional theory (DFT), one can expect Dirac nodal rings in the electronic band structure of β-PbO_2 if the spin-orbit coupling is neglected [4,6]. These Dirac nodal rings evolve into Dirac points due to spin-orbit coupling, but as long as the symmetry is described by the $P4_2/mnm$ space group, the Dirac points at the Γ-Z line remain, and the semimetallic state is symmetry protected, i.e., robust against spin-orbit coupling. However, if the crystal structure of β-PbO_2 is not described by $P4_2/mnm$ but one of its orthorhombic subgroups which does not contain the mirrors m_{110} and $m_{1\bar{1}0}$ and fourfold rotations around [001] with translation by $(1/2, 1/2, 1/2)$, then the semimetallic state is not protected. In orthorhombic symmetry the Dirac points disappear, resulting in an insulator state for β-PbO_2 [4,6]. DFT calculations presented in [4] suggest that β-PbO_2 is insulating with low symmetry (orthorhombic space group $Pnnm$) below 200 K and it is a semimetal with high symmetry (tetragonal rutile-type structure) above 200 K. Therefore, the determination of the crystal symmetry is an essential step for better understanding of the electronic properties of β-PbO_2.

With regard to the relationship of the symmetry properties one should highlight the behavior of β-PbO_2 at high pressures. Indeed, there is a second-order structural phase transition from tetragonal rutile type to orthorhombic $CaCl_2$ type ($P4_2/mnm \rightarrow Pnnm$) in β-PbO_2 at 4.0 GPa [8,27]. This phase transition is related to the optical vibrational mode described by the irreducible representation B_{1g} of the point group $4/mmm$ [28,29]. The high-symmetry (tetragonal) and low-symmetry (orthorhombic) structures are shown

*Piotr.Fabrykiewicz@fuw.edu.pl
†Corresponding author: radek@fuw.edu.pl

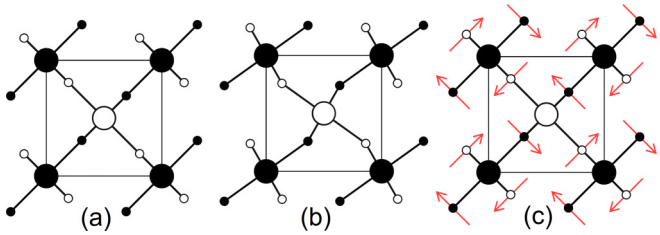

FIG. 1. Schematic view along the z axis of the (a) tetragonal and (b) orthorhombic unit cells of β-PbO_2. The Pb and O ions are shown with large and small circles, respectively. Solid and open symbols represent ions in the $z = 0$ and $z = 1/2$ planes, respectively. The deformation of Pb-O bond directions is exaggerated for visualization. (c) Eigenvectors of the B_{1g} optical mode of the oxygen anions are shown with arrows in the plane of the drawing.

schematically in Figs. 1(a) and 1(b), while the atomic displacements due to the B_{1g} optical mode are shown in Fig. 1(c).

A similar phase transition at high pressures has been observed in many other rutile-type oxides, e.g., β-MnO_2 [30] and SnO_2 [31], and fluorides, e.g., NiF_2 [11,32]. A measure of the degree of the distortion is given by the relative difference of lattice parameters, i.e.,

$$r_{ab} = 2\frac{a-b}{a+b}. \quad (1)$$

Between 4 and 21 GPa the degree of lattice distortion of β-PbO_2 increases with pressure [8,27]. At 7 GPa the values of r_{ab} were reported as being 0.010 for single crystals in [8] and 0.024 for powder samples in [27]. Our recent studies of β-MnO_2 [33] have shown that its crystal structure at ambient conditions is not tetragonal but orthorhombic (*Pnnm*) with the relative difference of lattice parameters $r_{ab} = 0.0021(1)$, i.e., about 10 times less than for β-PbO_2 at 7 GPa. The orthorhombic symmetry at ambient conditions is a possible scenario not only for β-PbO_2 but also for other rutile-type oxides. In this study we would like to show how the crystal structure of β-PbO_2 changes with temperature.

II. MATERIALS AND METHODS

Two commercial powder samples of β-PbO_2 provided by Acros, lot A0414657 (referred to as S1), and Alfa-Aesar, lot 23997 (referred to as S2), were used for both neutron and synchrotron radiation (SR) powder diffraction studies. The scattering vector length is defined as $Q = (2/\lambda)\sin\theta$ for wavelength λ and scattering angle 2θ.

The powder β-PbO_2 samples S1 and S2 were sealed in borosilicate capillaries with a 0.5-mm diameter for SR powder diffraction measurements using the Materials Science and Powder Diffraction (MSPD) beamline [34,35], ALBA-CELLS[1] Barcelona, with the MYTHEN detector configuration [36]. The x-ray wavelengths were calibrated with Si. In the first SR diffraction session with a wavelength

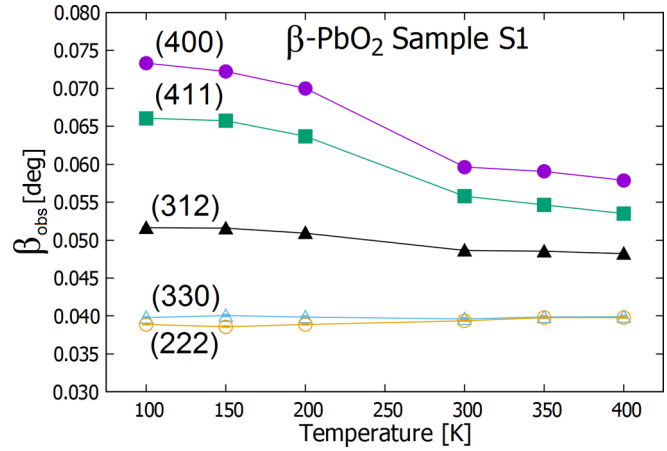

FIG. 2. Temperature dependence of the integral breadth β_{obs} of selected Bragg peaks (see text) observed for β-PbO_2 (sample S1) by SR powder diffraction using 0.44275(4)-Å wavelength. The statistical errors are smaller than the symbols. The lines are simply linking the points.

of 0.44275(4) Å both samples S1 and S2 were measured at 300 K. Sample S1 was measured also in the following sequence of temperatures: 300, 200, 150, 100, 300, 350, 400, and 450 K. In the second SR diffraction session with a wavelength of 0.41359(1) Å sample S2 was measured in the following sequence of temperatures: 100, 150, 200, 250, and 300 K. In both sessions the measured angular range was $5^\circ < 2\theta < 42^\circ$. This range corresponds to the scattering vector range $0.20 < Q < 1.60$ Å^{-1}. Data were collected using a cryostream 700+ series model from Oxford Cryosytems flowing thermalized N_2 gas on the sample in the beam. Temperature regulation and controls are made using supplier proprietary controller and alignment protocols.

Samples S1 and S2 were placed in 8-mm-diameter thin-walled vanadium containers for neutron powder diffraction measurements at the instrument D2B, Institut Laue-Langevin (ILL) Grenoble. The neutron wavelength at D2B was calibrated using the β-PbO_2 S1 sample measured at MSPD (300 K), giving a wavelength of 1.5946(1) Å. Measurements were performed at 300 and 100 K using open collimation in the angular range $10^\circ < 2\theta < 122^\circ$, corresponding to $0.11 < Q < 1.10$ Å^{-1}. Measurements were done with a standard ILL orange cryostat. The temperature in the cryostat was controlled using probes with Cernox thermometers (Cernox CX-1050) and a LakeShore Model 340.

We also analyzed x-ray powder diffraction data on another commercial β-PbO_2 sample studied by another group [12]. The authors of [12] provided us with the raw x-ray diffraction data measured with a Bruker AXS Advance (Cu $K\alpha$) for $10.0^\circ < 2\theta < 90.0^\circ$. This sample is denoted as M0 (see Fig. 3 below). All technical details related to the synthesis and x-ray diffraction measurements of sample M0 are given in [12].

The neutron, SR, and x-ray powder diffraction patterns were analyzed using two methods. The first method included fitting pseudo-Voigt functions to individual Bragg peaks and performing an analysis of the anisotropic peak broadening method as described in [33,37,38]. The second method was Rietveld analysis [39] of the whole powder pattern using

[1]CELLS stands for *Consorcio para la Construcción, Equipamiento y Explotación del Laboratorio de Luz de Sincrotrón, ang. Consortium for the Construction, Equipping and Exploitation of the Synchrotron Light Source*.

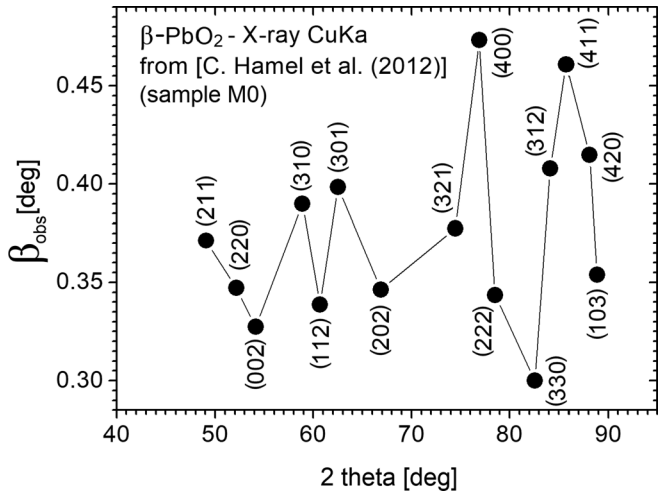

FIG. 3. Integral breadths β_{obs} observed for the Bragg peaks measured by x-ray (Cu $K\alpha$) diffraction for β-PbO_2 (M0); data were provided by the authors of Ref. [12]. The indices in the tetragonal setting are shown. The lines are shown to guide the eye.

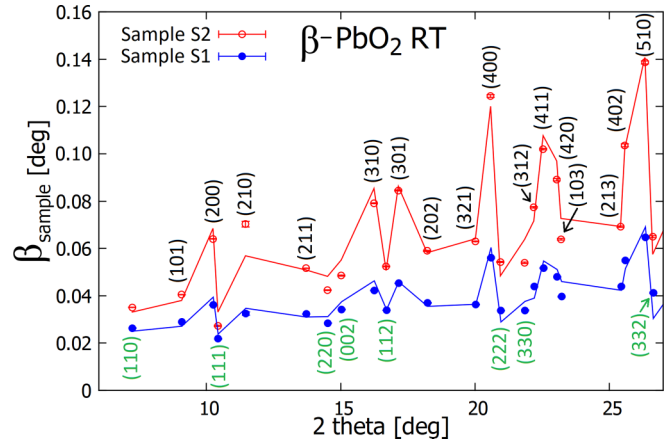

FIG. 4. Integral breadths observed for the Bragg peaks measured by SR diffraction for β-PbO_2, samples S1 and S2 at RT, using 0.44275(4)-Å wavelength, are shown with solid and open symbols, respectively. The refinement with the Stephens model [38], [see Eq. (2)] is shown with the solid line. The indices of Bragg peaks in the tetragonal setting are shown. Indices of peaks with $h = k$ are given in green below points, while other indices are given in black above points.

two structural models of β-PbO_2, the rutile-type tetragonal structure (space group $P4_2/mnm$) and the $CaCl_2$-type orthorhombic structure (space group $Pnnm$), with the JANA2006 software [40].

Calculations were carried out within the DFT formalism by using the QUANTUM ESPRESSO package [41,42]. The electronic ground state of each structure was calculated using the Perdew-Zunger (PZ) [43], Perdew-Burke-Ernzerhof (PBE) [44], and PBEsol (revised PBE) [45] exchange-correlation functionals and the projector augmented wave method [46]. We used a supercell approach with a Monkhorst-Pack **k**-point mesh of $16 \times 16 \times 16$ and a kinetic energy cutoff of 60 Ry for Brillouin zone sampling and expanding the wave functions, respectively. The ionic positions were optimized with a 0.0026 eV/Å tolerance for atomic forces.

The variable-cell molecular dynamics (MD) calculations were done using the damped Beeman dynamics with the Wentzcovitch extended Lagrangian [42]. The time step for molecular dynamics was chosen to be 70 in Rydberg atomic units. For each temperature, we performed a MD simulation that lasted 10 000 time steps (about 34 ps). The simulation was done using the PZ functional with no spin polarization and by starting with the orthorhombic ($CaCl_2$-type) structure of β-PbO_2 with space group $Pnnm$.

The elastic properties, phonon dispersion relations, and electronic band structures were calculated using the THERMO_PW package [47]. The bulk modulus B_0 and its pressure derivative B_0' were determined from the energy-volume relation (E-V) data. For this purpose, the obtained values of the total energy were fitted versus the unit cell volume using the Birch-Murnaghan equation of state. Results of DFT calculations correspond to the PZ functional (if not specified differently).

III. RESULTS

A. Neutron and SR diffraction studies of β-PbO_2

All β-PbO_2 powder diffraction patterns mentioned above can be indexed and refined using the rutile-type tetragonal structure, but there are some unusual effects in the temperature dependence of peak widths as shown in Fig. 2. The selected Bragg peaks (400), (222), (330), (312), and (411) located in the relatively narrow angular region $20.5^\circ < 2\theta < 22.6^\circ$ were fitted with a pseudo-Voigt function. The widths of (222) and (330) are practically constant vs temperature, while the widths of (400), (411), and (312) decrease with temperature increase, as seen in Fig. 2.

This nonstandard behavior of the Bragg peak widths in β-PbO_2 motivated us to perform an analysis of the anisotropic peak broadening as described by Popa [37] and Stephens [38]. The Bragg peaks due to the β-PbO_2 phase observed in the SR diffraction patterns of samples S1 and S2 as well as the x-ray diffraction pattern of M0 from [12] were refined with a pseudo-Voigt function by using the program WINPLOTR [48]. The Bragg peaks' integral breadths [49] $\beta(2\theta)$ are displayed for sample M0 in Fig. 3 and for samples S1 and S2 in Fig. 4. The (hkl) indices given in Figs. 3 and 4 correspond, like for Fig. 2, to the tetragonal setting. The peak widths observed for all three samples, M0, S1, and S2, exhibit a similar hkl-dependent behavior, suggesting orthorhombic symmetry; see, e.g., similar studies in [33].

TABLE I. Parameters of the Stephens model [38] obtained from the analysis of SR powder diffraction patterns of β-PbO_2 (at 300 K); see Eq. (2).

Parameter	Sample S1	Sample S2
H_o (deg)	0.0190(12)	0.0183(27)
A_0 (deg^2)	0.0145(22)	0.0791(140)
A_1 (deg^2 Å^{-4})	$61(7) \times 10^{-6}$	$387(32) \times 10^{-6}$
A_2 (deg^2 Å^{-4})	$-159(15) \times 10^{-6}$	$-935(70) \times 10^{-6}$
A_3 (deg^2 Å^{-4})	$37(22) \times 10^{-6}$	$-13(74) \times 10^{-6}$
A_4 (deg^2 Å^{-4})	$-168(15) \times 10^{-6}$	$-665(70) \times 10^{-6}$

TABLE II. Symmetry-allowed parameters of the tetragonal rutile-type crystal structure (space group $P4_2/mnm$ on the left) and the $CaCl_2$-type orthorhombic structure (space group *Pnnm* on the right). The bottom shows the relations between lattice parameters, coordinates, and anisotropic displacement factors in both space groups.

$P4_2/mnm$						*Pnnm*					
Ion	Position	Site symmetry	x	y	z	Ion	Position	Site symmetry	x	y	z
Pb	(2a)	*mmm*	0	0	0	Pb	(2a)	$2/m$	0	0	0
O	(4f)	*m*2*m*	x	x	0	O	(4g)	*m*	x	y	0
		$P4_2/mnm$						*Pnnm*			
Relations		$a = b,\ \ x[O] = y[O],$ $U_{11}[Pb] = U_{22}[Pb],\ \ U_{11}[O] = U_{22}[O]$						$a \neq b,\ \ x[O] \neq y[O],$ $U_{11}[Pb] \neq U_{22}[Pb],\ \ U_{11}[O] \neq U_{22}[O]$			

The integral breadths of Bragg peaks observed in SR powder diffraction data of β-PbO_2 were analyzed by the anisotropic peak broadening model from [37,38]. The instrumental contribution to peak widths was estimated by measuring the SR powder diffraction pattern of a $Na_2Ca_3Al_2F_{14}$ reference standard [50]. The integral breadths obtained from the $Na_2Ca_3Al_2F_{14}$ diffraction pattern were refined with a fourth-order polynomial function $\beta_{\text{instr}}(\theta)$. The experimental sample contribution to the integral breadth $\beta_{\text{sample}}(2\theta)$ was calculated as $\beta_{\text{sample}}(2\theta) = [\beta^2_{\text{obs}}(2\theta) - \beta^2_{\text{instr}}(2\theta)]^{1/2}$.

The observed sample contribution was refined by the anisotropic broadening model using the function

$$\beta_{\text{sample}}(\theta) = \frac{H_o}{\cos\theta} + \left\{A_0 + A_1\frac{(h^4+k^4)}{Q^4} + A_2\frac{h^2k^2}{Q^4} + A_3\frac{l^4}{Q^4} + A_4\frac{(h^2+k^2)l^2}{Q^4}\right\}^{\frac{1}{2}}\tan(2\theta/2), \quad (2)$$

where H_o and A_0 describe the average crystallite size and isotropic microstrain, respectively, while A_1, A_2, A_3, A_4 describe the anisotropic microstrains [38]. The scattering vector $Q = (2/\lambda)\sin(\theta)$. The solid line given for samples S1 and S2 in Fig. 4 represents the best fit using the anisotropic broadening model [37,38]. The values of parameters H_0 and A_i $(i = 1, \ldots, 4)$ from Eq. (2) obtained for β-PbO_2 (samples S1 and S2) are given in Table I. The peak widths of sample S2 are larger than the corresponding peak widths of sample S1, indicating the different microstructure of both samples.

The negative values of A_2 indicate an orthorhombic distortion of the tetragonal lattice (see, e.g., [33]). Such a distortion leads to a broadening of $(h0l)$-type Bragg peaks and to a narrowing of (hhl)-type peaks, as was already observed, e.g., in β-MnO_2 and MnF_2 [33]. The fit with six free parameters using Eq. (2) works well for 24 peaks, as visualized in Fig. 4. In fact the same fit also works well for the extended 2θ range with 58 peaks, as shown in Fig. SM1 in the Supplemental Material (SM) [51]. A list of peak width values with (hkl) indices is given in Table SM1 in the SM [51].

The Rietveld refinements were done by assuming the two structure models described in Table II. The pseudo-Voigt peak shape was used assuming a 2θ dependence of the individual Bragg peak widths $\text{FWHM}^2 = U\tan^2(\theta) + V\tan(\theta) + W$ (Gaussian contribution) and $\text{FWHM} = X\tan(\theta) + Y/\cos(\theta)$ (Lorentzian contribution). There were no peak broadening contributions due to crystallite shapes or anisotropic microstrains used in Rietveld refinements. Following earlier neutron diffraction studies (e.g., [10]), the atomic displacement parameters for both Pb and O were included in our refinements.

Rietveld refinements of SR diffraction data were also performed, but the absorption coefficient of β-PbO_2 calculated for x rays with a wavelength of 0.44275 Å [52] gives $\mu R \approx 4$ [52]. For such high values of $\mu R > 1$ the absorption corrections used in standard Rietveld codes do not work properly in particular for determining atomic positions and thermal parameters, as discussed in [53]. Moreover, the large difference in scattering strength for Pb and O as well leads to large uncertainties of the positions and anisotropic displacement parameters of oxygen. Therefore, we limit the analysis of Rietveld refinements of our SR diffraction

TABLE III. Lattice parameters a, b, c and oxygen coordinates $(x, y, 0)$ obtained by Rietveld refinements of neutron powder diffraction of β-PbO_2 at 300 and 100 K. The last column shows the fit quality indicator wRp.

	Space group	a (Å)	b (Å)	c (Å)	x	y	wRp (%)
S1, 300 K	$P4_2/mnm$	4.95452(11)	$= a$	3.38481(10)	0.3069(3)	$= x$	6.48
S1, 300 K	*Pnnm*	4.95701(21)	4.95141(24)	3.38478(8)	0.3079(13)	0.3058(14)	5.99
S2, 300 K	$P4_2/mnm$	4.95736(21)	$= a$	3.38821(18)	0.3068(4)	$= x$	6.49
S2, 300 K	*Pnnm*	4.96232(33)	4.95193(35)	3.38819(14)	0.3087(13)	0.3051(14)	5.42
S1, 100 K	$P4_2/mnm$	4.95198(15)	$= a$	3.38270(13)	0.3068(4)	$= x$	8.17
S1, 100 K	*Pnnm*	4.95518(27)	4.94838(29)	3.38267(11)	0.3078(14)	0.3061(15)	7.34
S2, 100 K	$P4_2/mnm$	4.95502(33)	$= a$	3.38621(27)	0.3068(6)	$= x$	9.31
S2, 100 K	*Pnnm*	4.96233(36)	4.94757(37)	3.38625(17)	0.3100(12)	0.3039(12)	6.68

TABLE IV. c/a ratio, unit cell volume, r_{ab}, and r_{xy} (see text) calculated for β-PbO_2 at 300 and 100 K with parameters from Table III.

	Space group	c/a	Volume (Å^3)	r_{ab}	r_{xy}	wRp (%)
S1, 300 K	$P4_2/mnm$	0.683176(24)	83.088(3)	0	0	6.48
S1, 300 K	$Pnnm$	0.683213(25)	83.077(5)	0.00113(7)	0.007(9)	5.99
S2, 300 K	$P4_2/mnm$	0.683470(45)	83.267(6)	0	0	6.49
S2, 300 K	$Pnnm$	0.683498(42)	83.258(9)	0.00210(10)	0.012(9)	5.42
S1, 100 K	$P4_2/mnm$	0.683100(33)	82.951(4)	0	0	8.17
S1, 100 K	$Pnnm$	0.683122(34)	82.943(7)	0.00137(9)	0.005(9)	7.34
S2, 100 K	$P4_2/mnm$	0.683390(71)	83.139(9)	0	0	9.31
S2, 100 K	$Pnnm$	0.683407(51)	83.137(10)	0.00298(10)	0.020(8)	6.68

patterns and x-ray diffraction patterns from [12] to the determination of only the lattice parameters and crystalline microstructure.

Both neutron and SR diffraction patterns of sample S1 show only Bragg peaks due to the β-PbO_2 phase. The patterns of sample S2 also have relatively weak peaks due to the orthorhombic α-PbO_2 phase [10]. The structural parameters of both phases were Rietveld refined for the neutron diffraction patterns of sample S2, giving β-PbO_2 (96 vol %) and α-PbO_2 (4 vol %). The structural parameters of the β-PbO_2 phase obtained by Rietveld refinements for both β-PbO_2 samples S1 and S2 obtained with neutron diffraction (D2B) at 100 and 300 K are given in Tables III and IV. Values of the fit quality indicator weighted-profile R-factor (wRp) clearly indicate the preference for the orthorhombic symmetry. Neutron diffraction patterns for samples S1 and S2 measured at 300 K are shown in Fig. SM3 in the SM [51].

Similar to r_{ab}, Eq. (1), the degree of distortion of the oxygen sublattice is quantified by r_{xy} calculated from oxygen coordinates $(x, y, 0)$:

$$r_{xy} = 2\frac{x-y}{x+y}. \tag{3}$$

In every refinement using orthorhombic symmetry of β-PbO_2 we obtain a positive sign for both r_{ab} and r_{xy} as reported in Table IV (we keep the convention to arbitrarily choose $a > b$ for the starting parameters, and in every case we get $x > y$ in the fit results). The same correlation of r_{ab} and r_{xy} signs was observed, e.g., in β-MnO_2 and MnF_2 [33] at ambient conditions and also in high-pressure studies, e.g., β-MnO_2 [30] or NiF_2 [32].

In a first step, we concentrate on the results of the tetragonal rutile-type structure fit in Table III: the lattice parameters of samples S1 and S2 differ considerably. Such differences in lattice parameters are not surprising because of the wide distribution of stoichiometry and defects of β-PbO_2 samples reported, e.g., in [16,18,23,25,26]. The present results are compared with other β-PbO_2 structural studies published in the literature (e.g., [7,10,13,16,17,19–22]). The tetragonal unit cell volumes $V = a^2c$ and the c/a ratios plotted in Fig. 5 highlight a relatively wide distribution (about 0.2% for c/a and 0.6% for V; see also Table V) across numerous β-PbO_2 materials. One can see that our samples S1 and S2 fit well in the trend of positive correlation, i.e., an increase of V with an increase of c/a shown by most of the data sets in Fig. 5. The values of the lattice parameters a and b of samples S1, S2, and M0 plotted in Fig. 6 confirm the orthorhombic distortion at 300 K. One should note that it is not straightforward to compare absolute values of lattice parameters extracted from measurements at different instruments. For both S1 and S2 samples the difference $a - b$ decreases with increasing temperature above 200 K (see Fig. 6). This is the main reason of the specific temperature changes of

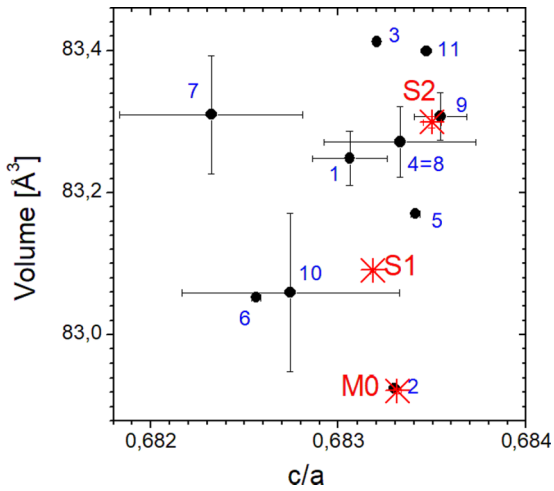

FIG. 5. Values of the tetragonal lattice parameter ratio c/a and unit cell volume $V = a^2c$ for β-PbO_2 published between 1926 and 2019 (with references given in Table V) are shown by solid circles. The present results for samples S1 and S2 as well as M0 [12] samples are shown by stars.

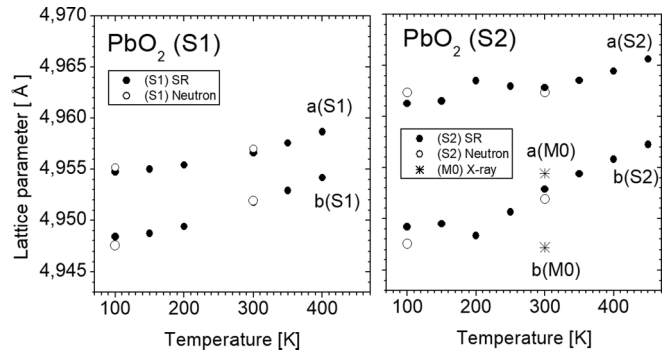

FIG. 6. Temperature dependence of the β-PbO_2 lattice parameters a and b in the orthorhombic setting of space group $Pnnm$ for sample S1 (left panel) and sample S2 (right panel). The results from RT x-ray studies of sample M0 [12] are shown by stars. The errors are about the size of the symbol.

TABLE V. Tetragonal lattice parameters a, c and references for β-PbO_2 structural studies numbered from 1 to 11 as in Fig. 5. Battery-related β-Pb_xO_2 samples from [10,18] reported lead stoichiometry of $0.95 < x < 1$.

No.	a (Å)	c (Å)	Method	Author(s) and year	Ref.	Remarks
M0	4.9509(1)	3.3830(1)	x-ray	Hamel *et al.* (2012)	[12]	with present analysis also
1	4.958(1)	3.3867(7)	x-ray	Paulsen *et al.* (2019)	[7]	single crystal
2	4.951	3.383	neutron	Scanlon *et al.* (2011)	[16]	
3	4.9606	3.3893	x-ray	Taylor (1984)	[17]	
4	4.9578(2)	3.3878(2)	neutron	Jorgensen *et al.* (1982)	[18]	
5	4.9556(1)	3.3867(1)	neutron	Hill (1982)	[10]	chemically prepared
6	4.9553(1)	3.3823(1)	neutron	Hill (1982)	[10]	acid electroformed
7	4.961(2)	3.385(2)	x-ray	Harada *et al.* (1981)	[19]	
8	4.9578(2)	3.3878(2)	neutron	D'Antonio and Santoro (1980)	[20]	
9	4.958(1)	3.389(1)	x-ray	Syono and Akimoto (1968)	[21]	
10	4.955(3)	3.383(2)	neutron	Leciejewicz and Padło-Sosnowska (1962)	[13]	
11	4.96	3.39	x-ray	Goldschmidt *et al.* (1926)	[22]	

the Bragg peak widths displayed in Fig. 2. In order to visualize this effect we have represented the integral breadths of Bragg peaks measured with SR powder diffraction for β-PbO_2 (sample S1) at temperatures from 100 to 400 K. Results for selected angular ranges are shown in Fig. 7, while a similar figure with the full 2θ range is given by Fig. SM2 in the SM [51].

It is important to point out the present result: despite different lattice parameters, different microstructures, and possibly different stoichiometries, all studied samples, i.e., S1, S2, and M0, exhibit the orthorhombic $CaCl_2$-type structure at ambient temperature and pressure.

The anisotropic displacement parameters in the orthorhombic symmetry allow for different values of U_{11} and U_{22} for both Pb and O ions, as explained in Table II. The resulting U_{ij} values obtained from neutron diffraction patterns of β-PbO_2 are given in Table VI. In both samples S1 and S2 we obtain $U_{22} > U_{11}$, and this anisotropy is more pronounced at 300 K than at 100 K. The elongation of U_{22} vs U_{11} could be due to lattice vibrations, but it could also be a sign of the directional preference for transport phenomena, e.g., ionic conductivity or hydrogen diffusion. Most hydrogen diffusion measurements were done on polycrystalline β-PbO_2 samples (e.g., [54]), and their possible directional character is, at present, only a hypothesis.

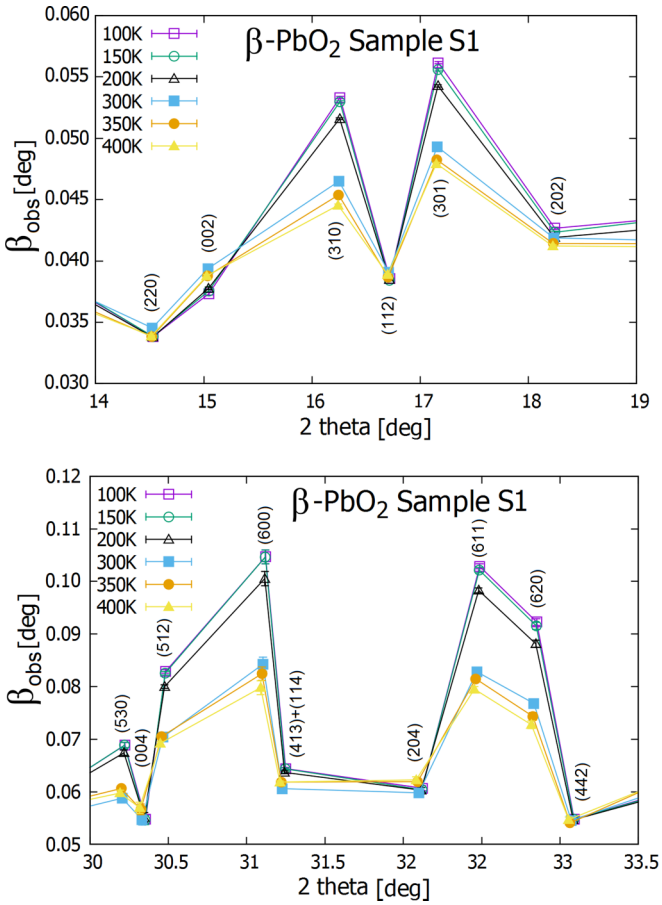

FIG. 7. Integral breadths β_{obs} vs 2θ of several Bragg peaks observed for β-PbO_2 (sample S1) by SR powder diffraction, using 0.44275(4)-Å wavelength, at several temperatures are shown with tetragonal indices. The statistical errors are smaller than the symbols, and the lines are simply linking the points.

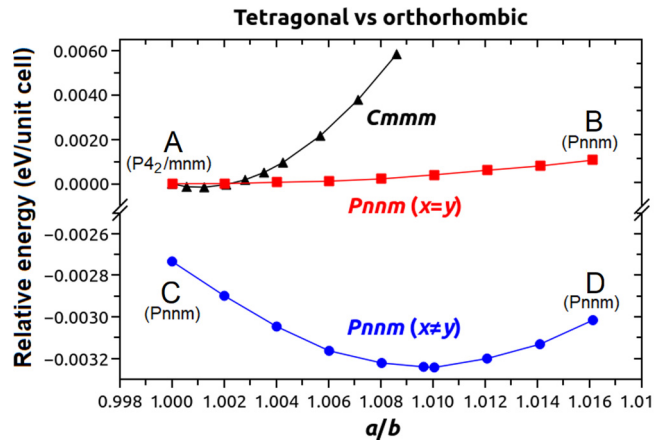

FIG. 8. The relative energy (in eV/2 f.u.) of β-PbO_2 at *Pnnm* and *Cmmm* symmetries is shown as a function of the lattice constant ratio a/b. β-PbO_2 described by the red dots has *Pnnm* symmetry with the exception of the $a = b$ case, for which it turns into tetragonal ($P4_2/mnm$) symmetry.

TABLE VI. Anisotropic displacement parameters (in Å^2) of β-PbO_2 (samples S1 and S2) determined by Rietveld refinement of neutron powder diffraction data at 100 and 300 K.

	Pb				
Sample	U_{eq}	U_{11}	U_{22}	U_{33}	U_{12}
S1, 300 K	0.0041(10)	−0.0002(19)	0.0107(24)	0.0018(7)	−0.0007(7)
S1, 100 K	0.0007(12)	−0.0020(22)	0.0052(26)	−0.0011(9)	0.0004(8)
S2, 300 K	0.0055(11)	0.0016(19)	0.0099(23)	0.0021(9)	−0.0003(9)
S2, 100 K	0.0016(10)	0.0044(20)	0.0059(21)	-0.0028(11)	0.0007(10)
	O				
Sample	U_{eq}	U_{11}	U_{22}	U_{33}	U_{12}
S1, 300 K	0.0079(14)	0.0079(28)	0.0117(30)	0.0040(10)	−0.0074(9)
S1, 100 K	0.0035(15)	0.0038(31)	0.0048(31)	0.0020(13)	−0.0040(11)
S2, 300 K	0.0090(14)	0.0101(28)	0.0123(29)	0.0046(13)	−0.0077(12)
S2, 100 K	0.0045(13)	0.0059(26)	0.0051(26)	0.0024(16)	−0.0034(14)

B. First-principles calculations: Search for the optimal structure of β-PbO_2

The preliminary target of our first-principles calculations is to determine the optimized lattice parameters of β-PbO_2 in the $P4_2/mnm$ and $Pnnm$ symmetries by using the widely used exchange-correlation functionals like PBE, PZ, and PBEsol. The results of the calculations are given in Table VII. The lattice parameters collected in Table VII all agree within 3% with the corresponding low-temperature (100 K) experimental values for β-PbO_2. PBEsol gives results similar to PBE and PZ, confirming the correctness of our approach.[2]

The best agreement is obtained within the standard local-density approximation (LDA), i.e., the PZ functional. The values of r_{ab} and r_{xy} obtained with the three DFT approaches are close to each other (see Table VII) but are overestimated compared with the experimental values. It should be pointed out that in terms of total energy, all the DFT methods used here give preference to β-PbO_2 at $Pnnm$ with respect to $P4_2/mnm$ symmetry.

The DFT calculations on the possible tetragonal and orthorhombic crystal structures of β-PbO_2 was done in the following steps:

(i) The tetragonal structure has $a = b$ and oxygen coordinates $x = y$ compatible with $P4_2/mnm$ (as shown schematically in Table VIII, structure A). In our scale of energy this state has $E = 0$, and it is shown in Fig. 8 as point A.

(ii) The orthorhombic structure has $a \neq b$ but with oxygen atoms lying in the $(1, \bar{1}, 0)$ plane, i.e., oxygen coordinates $x = y$, compatible with the space group $Pnnm$ (as reported schematically in Table VIII, structure B). There is a saddle point at the $(1, \bar{1}, 0)$ plane, so during DFT calculations the oxygen coordinates remain constant: $x = y$ for any r_{ab} value. The relative energy of these states (per 2 f.u.) is shown in Fig. 8 along the line AB.

(iii) The orthorhombic structure has $a = b$ but oxygen coordinates $x \neq y$. The unit cell fits to the tetragonal setting, i.e., $a = b$, but due to oxygen coordinates this structure is

[2]The PBEsol functional is known to describe correctly, e.g., the relative total energy of cubic and hexagonal polymorphs of boron nitride for which standard LDA, generalized gradient approximation, and hybrid functionals were unable to reproduce the correct sequence of total energies of the two phases [55].

TABLE VII. Theoretical lattice parameters, oxygen coordinates $(x, y, 0)$, r_{ab} and r_{xy} (see text), and total and relative energy values for β-PbO_2 at $Pnnm$ and $P4_2/mnm$ symmetries (total energies are given per 2 f.u.). Results of calculations using three different exchange-correlation functionals are shown.

	PBE		PBEsol		PZ		Expt. (100 K)
	$Pnnm$	$P4_2/mnm$	$Pnnm$	$P4_2/mnm$	$Pnnm$	$P4_2/mnm$	$Pnnm$
a (Å)	5.090	5.064	5.000	4.985	4.962	4.947	4.9552(3)
b (Å)	5.028	5.064	4.952	4.985	4.915	4.947	4.9484(3)
c (Å)	3.450	3.454	3.418	3.422	3.400	3.403	3.3827(1)
r_{ab}	0.012	0	0.010	0	0.010	0	0.0014(1)
x	0.325	0.308	0.330	0.308	0.328	0.307	0.3078(14)
y	0.291	0.308	0.285	0.308	0.287	0.307	0.3061(15)
r_{xy}	0.111	0	0.144	0	0.134	0	0.005(9)
E_{tot} (Ry)	−1907.53210752	−1907.53208152	−1883.29644642	−1883.29634814	−1859.21813648	−1859.21791215	
ΔE_{tot} (meV)	0.4		1.3		3.1		
E_g (meV)	143 (HSE06: 525)	0	191	0	182	0	610 after [56]

TABLE VIII. Schematic presentation of the four crystal structures of β-PbO_2 used in DFT calculations (see text), one with tetragonal $P4_2/mnm$ symmetry (A) and three with orthorhombic $Pnnm$ symmetry (B–D).

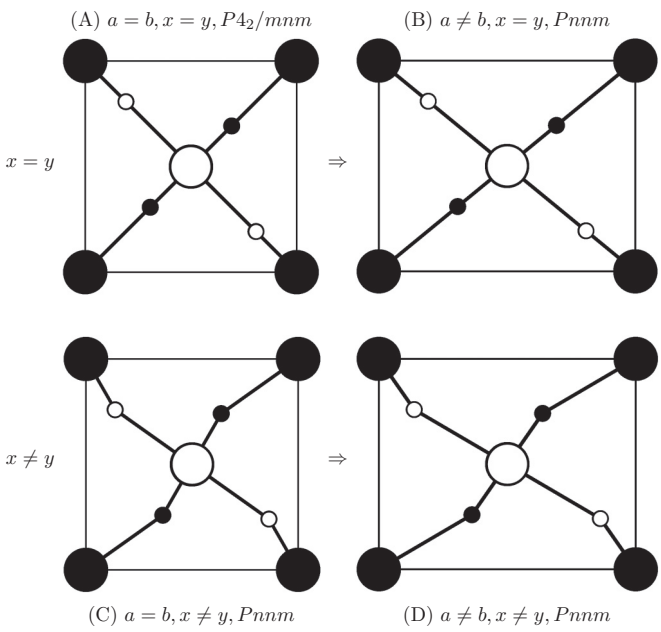

described by the space group *Pnnm* (as shown schematically in Table VIII, structure C). The energy of these states is shown in Fig. 8 as point C.

(iv) Orthorhombic symmetry (*Pnnm*) has both $a \neq b$ and oxygen coordinates, i.e., $x \neq y$ (as shown schematically in Table VIII, structure D). The energy of these states is shown in Fig. 8 along the line CD.

Results of DFT calculations (at zero temperature; see Fig. 8) confirm that the orthorhombic symmetry is the most likely one for β-PbO_2. Even with equal lattice parameters $a = b$ the orthorhombic configuration (point C; $x \neq y$; in Fig. 8) is lower in total energy by 2.7 meV than the tetragonal one (point A). The lowest-energy (orthorhombic) structure is more stable by 3.2 meV than the tetragonal one. The minimum total energy calculated with DFT corresponds to the lattice parameter $r_{ab} \approx 0.010$, i.e., 3–6 times more than the values obtained in our measurements with samples S1 and S2: 0.0014 and 0.0030, respectively (see Table IV).

TABLE IX. Calculated Raman active modes (in cm^{-1}) for β-PbO_2 at *Pnnm* and $P4_2/mnm$ symmetries, compared to the experiment reported in Ref. [57]. The values given in parentheses are suggested in the experiment to arise from trace amounts of Pb_3O_4.

		E_g	A_{1g}	B_{2g}
$P4_2/mnm$		399	540	652
	B_{3g}	B_{2g}	A_g	B_{1g}
Pnnm	390	396	528	645
Experiment	(390)	424	515 (546)	653

Test DFT calculations were also done for a few unlikely deformations which were never reported in experimental studies of β-PbO_2, i.e., the orthorhombic *Cmmm* structure (shown in Fig. SM4(a) in the SM [51]) and modifications of the *Pnnm* structure with oxygen positions breaking the inversion symmetry (shown in Figs. SM4(b) and SM4(c) in the SM [51]). DFT calculations with the *Cmmm* structure give significantly higher total energies than the tetragonal one (see Fig. 8). Moreover, calculations for noncentrosymmetric structures converged to the orthorhombic *Pnnm* structure corresponding to the total energy minimum in line CD in Fig. 8.

C. Properties of the optimal structure of β-PbO_2

The physical properties of the orthorhombic *Pnnm* phase of β-PbO_2 found with DFT calculations are compared with available experimental data related to lattice dynamics, thermal expansion, and elastic properties.

The structural stability of β-PbO_2 at tetragonal and orthorhombic symmetries is studied by examining the phonon dispersion relations which are represented in Fig. 9. We confirm that β-PbO_2 at $P4_2/mnm$ is dynamically unstable due to the existence of the B_{1g} soft mode, shown in Fig. 1. Similar results were reported for β-PbO_2 using PBE in Ref. [4]. One can see in Fig. 9 (left) negative frequencies of the B_{1g} mode around

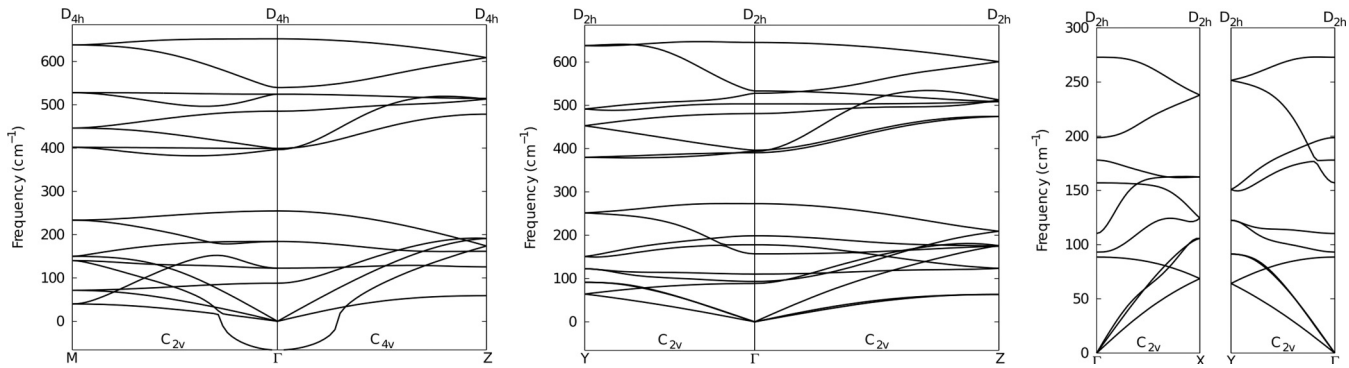

FIG. 9. Phonon dispersion relations calculated with DFT for tetragonal (left) and orthorhombic (middle and right) phases of β-PbO_2. Phonon dispersion for the tetragonal phase is given along the M-Γ-Z line, while that for the orthorhombic phase is along the Y-Γ-Z, Γ-X, and Y-Γ lines. The point group symmetry of each **q** point or path is indicated by labels. The phonon dispersion relations for the remaining parts of the Brillouin zone are shown in Fig. SM5 in the SM [51].

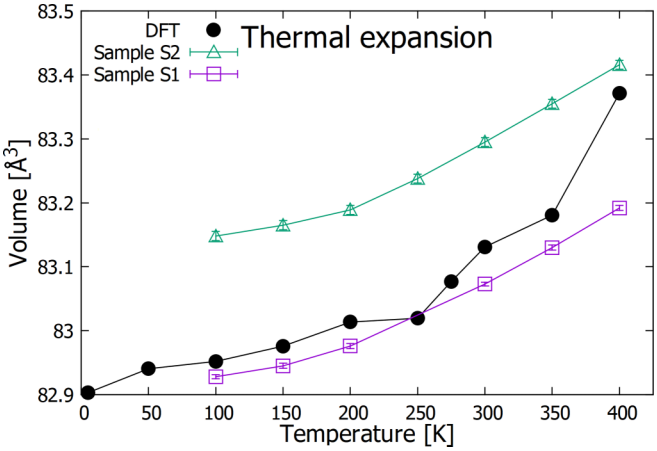

FIG. 10. Temperature dependence of the unit cell volume of β-PbO_2 at *Pnnm* symmetry calculated with DFT (solid symbols) and measured for samples S1 and S2 with SR powder diffraction (open symbols).

the Γ point in tetragonal β-PbO_2, while this soft mode is no longer present in the orthorhombic structure of β-PbO_2 (see Fig. 9, middle). The acoustic modes along the Γ-X direction have higher frequencies than those along the Γ-Y direction (see Fig. 9, right); that is, the orthorhombic β-PbO_2 lattice is stiffer along the a direction than along the b direction.

We compare calculations of the frequencies of the Raman active phonon modes with experimental results from [57] in Table IX. There is satisfactory agreement, confirming the correctness of the DFT methodology.

The β-PbO_2 volume thermal expansion is evaluated using first-principles molecular dynamic simulations, as shown in Fig. 10. The $V(T)$ curve calculated with molecular dynamics follows correctly the experimental trend. The average volume at a given temperature is further used to evaluate the symmetry of β-PbO_2 at finite temperatures. For each temperature, we obtain positive values of r_{ab} and r_{xy}, pointing to the orthorhombic symmetry of β-PbO_2.

The elastic constants C_{ij} calculated with DFT for the tetragonal and orthorhombic β-PbO_2 structures (at zero pressure and zero temperature) are presented in Table X. Our results are compared with calculations of other groups done for only the tetragonal phase [58–60]. We include in Table X our results obtained using the PZ and PBE exchange-correlation functionals. Our calculations show that β-PbO_2 in the *Pnnm* symmetry is softer in the b direction than in the a direction since $C_{11} > C_{22}$ by 23% (PBE: 9%). This is consistent with the observed temperature variation of the lattice constants shown in Fig. 6, i.e., larger thermal expansion along the b axis than along the a axis. This is also consistent with the anisotropic displacement parameters for Pb in β-PbO_2 reported in Table VI: the displacement parameter for Pb atoms is clearly larger in the b direction than in the a direction ($U_{22} > U_{11}$).

TABLE XI. The bulk modulus B (in GPa) calculated from the elastic constants using the Voigt and Reuss approximation methods and the bulk modulus B_0 and its pressure derivative B_0' obtained by fitting the energy-volume data to the Birch-Murnaghan equation of state compared to available experimental data [8]. We have done a reanalysis of the data from [8,61] (more details are given in Fig. SM7 in the SM [51]).

	B_V	B_R	B_0	B_0'
$P4_2/mnm$ (DFT)	153	141	148	4.4
Pnnm (DFT)	123	106	122	5.0
Experiment (reanalysis [8,61])			119	4.5

The bulk modulus values calculated for the tetragonal and orthorhombic β-PbO_2 phases are given in Table XI. The experimental value of the bulk modulus obtained by our reanalysis of the data from [8,61] is close to the values calculated for the orthorhombic model. Details of the β-PbO_2 compressibility studies by [8,61] are explained in Fig. SM7 in the SM [51]. In the present case all three DFT functionals overestimate the lattice constants (see Table VII) and therefore underestimate the bulk modulus as observed for most solids (e.g., [62]). Consequently, the values of B_0 given in Table XI are more likely underestimated for both β-PbO_2 structures. Having this in mind, the DFT result for the orthorhombic structure matches better the experimental value for B_0 (see Table XI).

The lowering in symmetry also influences the electronic structure of β-PbO_2. This is evidenced in Fig. 11, where the left and right panels display results for the tetragonal and orthorhombic phases, respectively. In the left panel the Fermi energy crosses the band structure at the Γ-Z high-symmetry line; therefore, β-PbO_2 in the $P4_2/mnm$ symmetry is a symmetry-protected metal. However, the symmetry of

TABLE X. Elastic constants C_{ij} (in GPa) of β-PbO_2 calculated using PBE and PZ exchange-correlation functionals at *Pnnm* and $P4_2/mnm$ symmetries, compared with the available theoretical data.

C_{11}	C_{22}	C_{33}	C_{12}	C_{13}	C_{23}	C_{44}	C_{55}	C_{66}	a, b	c	Method	Ref.
						$P4_2/mnm$						
161.7	161.7	289.5	101.9	96.9	96.9	71.9	71.9	154.5	4.836, 4.836	3.302	PBE	[58]
159.8	159.8	285.4	124.8	130.2	130.2	47.6	47.6	148.5	4.947, 4.947	3.403	PZ	this work
131.4	131.4	239.5	96.0	104.1	104.1	40.8	40.8	127.9	5.064, 5.064	3.454	PBE	this work
131	131	242	92	103	103	38	38	125	5.082, 5.082	3.449	PBE	[59]
106.8	106.8	225.8	74.0	90.7	90.7	32.9	32.9	111.0	5.195, 5.195	3.454	PBE	[60]
						Pnnm						
157.9	122.0	254.2	77.7	80.4	128.6	42.8	54.4	144.0	4.962, 4.915	3.400	PZ	this work
111.5	101.8	228.1	104.0	98.7	83.7	27.3	36.6	125.4	5.090, 5.028	3.450	PBE	this work

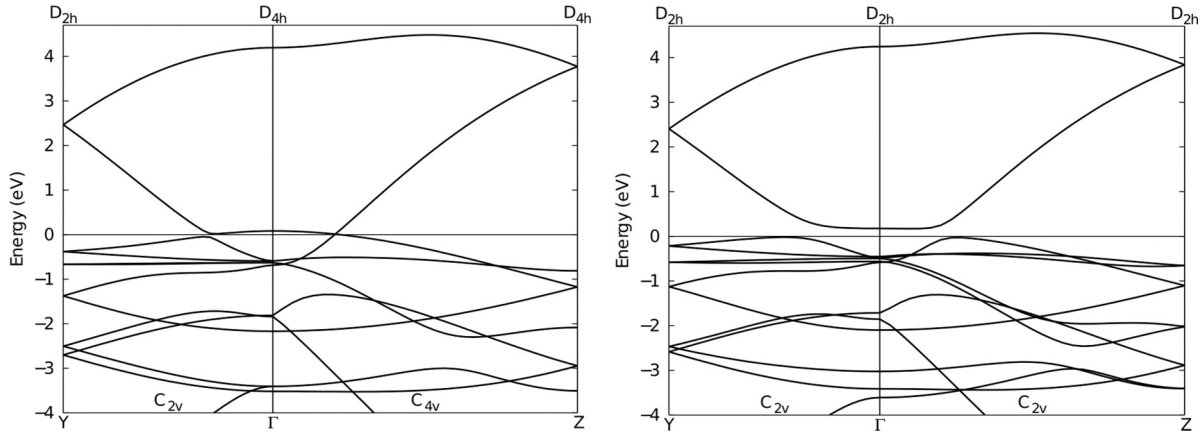

FIG. 11. Electronic band structure for tetragonal (left) and orthorhombic (right) β-PbO_2. To facilitate the comparison between the two cases, β-PbO_2 at $P4_2/mnm$ symmetry is treated as orthorhombic with $a = b$, and the same k path in the Brillouin zone is followed for both cases. The point group symmetry of each **k** point or path is indicated by labels. The electronic structure calculated for the remaining parts of the Brillouin zone are shown in Fig. SM6 in the SM [51].

the Γ-Z line changes from C_{4v} in the tetragonal case to C_{2v} in the orthorhombic case (see Fig. 11, right panel), and as a result β-PbO_2 in the *Pnnm* symmetry is a semiconductor (i.e., it is no longer symmetry protected according to [6]) with a band gap of about 0.2 eV. Similar results are also obtained with PBE and PBEsol (see Table VII). This is in accord with the experiment [56], which reports a band gap of 0.6 eV. To account better for the band gap value of β-PbO_2, we have recalculated the band gap of orthorhombic β-PbO_2 using the Heyd-Scuseria-Ernzerhof (HSE06) exchange-correlation functional [63]. We have obtained a value of 0.5 eV, which matches the experimental value much better than the corresponding HSE06 value of 0.2 eV reported recently [64] for the tetragonal phase of β-PbO_2.

IV. CONCLUSIONS

Neutron and SR diffraction studies as well as DFT calculations demonstrate that β-PbO_2 has an orthorhombic $CaCl_2$-type structure at temperatures from 100 to 400 K. The recent DFT calculations from [4] suggesting a phase transition from the insulating low-symmetry phase to the semimetal high-symmetry phase at 200 K are not supported by our results. Our studies highlighted different thermal expansion coefficients and different anisotropic displacement parameters along the a and b directions ($a > b$) in β-PbO_2. DFT calculated frequencies of the Raman active phonon modes agree with the experimental results from [57]. Calculations evidence that β-PbO_2 is softer in the b direction than in the a direction ($a > b$) as $C_{11} > C_{22}$. This result is also consistent with the larger thermal expansion along b axis than along the a axis and the anisotropic displacement parameters being larger in the b direction than in the a direction (U_{22}[Pb] > U_{11}[Pb]). From these observations one can expect the anisotropy of other physical properties of β-PbO_2, e.g., thermal and ionic conductivity and the hydrogen diffusion process. It is also possible to expect similar anisotropic properties of other rutile-type systems, e.g., β-MnO_2 and MnF_2 [33].

ACKNOWLEDGMENTS

Thanks are due to D. Guay (INRS-Énergie, Varennes, Québec) for providing x-ray diffraction data from his β-PbO_2 sample [12]. Thanks are due to D. Oleszak (Warsaw University of Technology) for help with x-ray diffraction characterization. We acknowledge the Ministry of Science and Higher Education (Poland) for funding. Numerical calculations were performed at the Interdisciplinary Centre for Mathematical and Computational Modelling (ICM) at the University of Warsaw under Grant No. GB80-23. We acknowledge provision of beamtime on BL04-MSPD at ALBA through In House proposal Proposal No. 2020104796. Thanks are due to the Ministry of Science (Poland) for funding access to the Institut Laue Langevin.

[1] G. Planté, Nouvelle pile secondaire d'une grande puissance, C. R. Hebd. Seances Acad. Sci. **50**, 640 (1860).
[2] M. Z. Hasan and C. L. Kane, Colloquium: Topological insulators, Rev. Mod. Phys. **82**, 3045 (2010).
[3] X.-L. Qi and S.-C. Zhang, Topological insulators and superconductors, Rev. Mod. Phys. **83**, 1057 (2011).
[4] T. Chen, D. Shao, P. Lu, X. Wang, J. Wu, J. Sun, and D. Xing, Anharmonic effect driven topological phase transition in PbO_2 predicted by first-principles calculations, Phys. Rev. B **98**, 144105 (2018).
[5] B. Peng, I. Bravić, J. L. MacManus-Driscoll, and B. Monserrat, Topological semimetallic phase in PbO_2 promoted by temperature, Phys. Rev. B **100**, 161101(R) (2019).
[6] S.-Y. Yang, H. Yang, E. Derunova, S. S. P. Parkin, B. Yan, and M. N. Ali, Symmetry demanded topological nodal-line materials, Adv. Phys.: X **3**, 1414631 (2018).
[7] C. Paulsen, C. Benndorf, J. Kösters, V. Galéa-Clolus, P. Clolus, R.-D. Hoffmann, and R. Pöttgen, Tetravalent lead in nature–plattnerite crystals from Mine du Pradet (France) and Mount Trevasco (Italy), Z. Naturforsch. B **74**, 427 (2019).

[8] E. Huang, A. S. Li, and S.-C. Yu, Compression studies of single-crystal SnO_2 and PbO_2 in a diamond cell, Terr., Atmos. Oceanic Sci. J. **3**, 111 (1992).

[9] T. Mahalingam, S. Velumani, M. Raja, S. Thanikaikarasan, J. Chu, S. Wang, and Y. Kim, Electrosynthesis and characterization of lead oxide thin films, Mater. Charact. **58**, 817 (2007).

[10] R. Hill, The crystal structures of lead dioxides from the positive plate of the lead/acid battery, Mater. Res. Bull. **17**, 769 (1982).

[11] W. H. Baur, The rutile type and its derivatives, Crystallogr. Rev. **13**, 65 (2007).

[12] C. Hamel, T. Brousse, D. Bélanger, and D. Guay, Effect of ball-milling on the physical and electrochemical properties of PbO_2 and $PbO_2/BaSO_4$ nanocomposite, J. Electrochem. Soc. **159**, A60 (2012).

[13] J. Leciejewicz and I. Padło-Sosnowska, Note on the oxygen parameter in tetragonal PbO_2, Naturwissenschaften **49**, 373 (1962).

[14] I. Padło-Sosnowska, Wyznaczenie parametru tlenowego w PbO_2 przy pomocy metody dyfrakcji neutronów, M.S. thesis, University of Warsaw, 1962.

[15] J. Leciejewicz and I. Padło-Sosnowska, The oxygen parameter in PbO_2 determined by neutron diffraction, Technical Report No. 27 3/I-N, Institute of Nuclear Research, Polish Academy of Sciences, 1961 (unpublished).

[16] D. O. Scanlon, A. B. Kehoe, G. W. Watson, M. O. Jones, W. I. F. David, D. J. Payne, R. G. Egdell, P. P. Edwards, and A. Walsh, Nature of the Band Gap and Origin of the Conductivity of PbO_2 Revealed by Theory and Experiment, Phys. Rev. Lett. **107**, 246402 (2011).

[17] D. Taylor, Thermal expansion data. II: Binary oxides with the fluorite and rutile structures, MO_2, and the antifluorite structure, M_2O Trans. J. Br. Ceram. Soc. **83**, 32 (1984).

[18] J. D. Jorgensen, R. Varma, F. J. Rotella, G. Cook, and N. P. Yao, Lead deficiency and hydrogen content in battery electrode β-PbO_2, J. Electrochem. Soc. **129**, 1678 (1982).

[19] H. Harada, Y. Sasa, and M. Uda, Crystal data for β-PbO_2, J. Appl. Crystallogr. **14**, 141 (1981).

[20] P. D'Antonio and A. Santoro, Powder neutron diffraction study of chemically prepared β-lead dioxide, Acta Crystallogr., Sect. B **36**, 2394 (1980).

[21] Y. Syono and S. Akimoto, High pressure synthesis of fluorite-type PbO_2, Mater. Res. Bull. **3**, 153 (1968).

[22] V. M. G. Goldschmidt, T. Barth, D. Holmsen, G. Lunde, and W. Zachariasen, Geochemische Verteilungsgesetze der Elemente; VI. Über die Krystallstrukturen vom Rutiltypus, mit Bemerkungen zur Geochemie Zweiwertiger und vierwertiger Element, Skrifter Norske Videnskaps-Akad. Oslo I. Mat.-Naturv. Kl. 1926, No. 1 (1926).

[23] M. Heinemann, H. J. Terpstra, C. Haas, and R. A. de Groot, Electronic structure of β-PbO_2 and its relation with $BaPbO_3$, Phys. Rev. B **52**, 11740 (1995).

[24] D. J. Payne, R. G. Egdell, W. Hao, J. S. Foord, A. Walsh, and G. W. Watson, Why is lead dioxide metallic?, Chem. Phys. Lett. **411**, 181 (2005).

[25] A. Walsh, A. B. Kehoe, D. J. Temple, G. W. Watson, and D. O. Scanlon, PbO_2: From semi-metal to transparent conducting oxide by defect chemistry control, Chem. Commun. **49**, 448 (2013).

[26] P. Rüetschi, Influence of crystal structure and interparticle contact on the capacity of PbO_2 electrodes, J. Electrochem. Soc. **139**, 1347 (1992).

[27] J. Haines, J. M. Léger, and O. Schulte, The high-pressure phase transition sequence from the rutile-type through to the cotunnite-type structure in β-PbO_2, J. Phys.: Condens. Matter **8**, 1631 (1996).

[28] J. F. Scott, Soft-mode spectroscopy: Experimental studies of structural phase transitions, Rev. Mod. Phys. **46**, 83 (1974).

[29] A. Mirgorodsky and M. Smirnov, Soft modes and proper ferroelasticity-3: Rutile-NiF_2, Ferroelectrics **159**, 151 (1994).

[30] J. Haines, J. Léger, and S. Hoyau, Second-order rutile-type to $CaCl_2$-type phase transition in β-MnO_2 at high pressure, J. Phys. Chem. Solids **56**, 965 (1995).

[31] H. Hellwig, A. F. Goncharov, E. Gregoryanz, H.-K. Mao, and R. J. Hemley, Brillouin and Raman spectroscopy of the ferroelastic rutile-to-$CaCl_2$ transition in SnO_2 at high pressure, Phys. Rev. B **67**, 174110 (2003).

[32] J. D. Jorgensen, T. G. Worlton, and J. C. Jamieson, Pressure-induced strain transition in NiF_2, Phys. Rev. B **17**, 2212 (1978).

[33] P. Fabrykiewicz, R. Przeniosło, I. Sosnowska, F. Fauth, and D. Oleszak, Verification of the de Wolff hypothesis concerning the symmetry of β-MnO_2, Acta Crystallogr., Sect. A **75**, 889 (2019).

[34] F. Fauth, R. Boer, F. Gil-Ortiz, C. Popescu, O. Vallcorba, I. Peral, D. Fullà, J. Benach, and J. Juanhuix, The crystallography stations at the Alba synchrotron, Eur. Phys. J. Plus **130**, 160 (2015).

[35] F. Fauth, I. Peral, C. Popescu, and M. Knapp, The new material science powder diffraction beamline at ALBA synchrotron, Powder Diffr. **28**, S360 (2013).

[36] A. Bergamaschi, A. Cervellino, R. Dinapoli, F. Gozzo, B. Henrich, I. Johnson, P. Kraft, A. Mozzanica, B. Schmitt, and X. Shi, The MYTHEN detector for X-ray powder diffraction experiments at the Swiss Light Source, J. Synchrotron Radiat. **17**, 653 (2010).

[37] N. C. Popa, The (*hkl*) dependence of diffraction-line broadening caused by strain and size for all Laue groups in rietveld refinement, J. Appl. Crystallogr. **31**, 176 (1998).

[38] P. Stephens, Phenomenological model of anisotropic peak broadening in powder diffraction, J. Appl. Crystallogr. **32**, 281 (1999).

[39] H. M. Rietveld, A profile refinement method for nuclear and magnetic structures, J. Appl. Crystallogr. **2**, 65 (1969).

[40] V. Petříček, M. Dušek, and L. Palatinus, Crystallographic Computing System JANA2006: General features, Z. Kristallogr. **229**, 345 (2014).

[41] P. Giannozzi *et al.*, QUANTUM ESPRESSO: A modular and open-source software project for quantum simulations of materials, J. Phys.: Condens. Matter **21**, 395502 (2009).

[42] P. Giannozzi *et al.*, Advanced capabilities for materials modeling with Quantum ESPRESSO, J. Phys.: Condens. Matter **29**, 465901 (2017).

[43] J. P. Perdew and A. Zunger, Self-interaction correction to density-functional approximations for many-electron systems, Phys. Rev. B **23**, 5048 (1981).

[44] J. P. Perdew, K. Burke, and M. Ernzerhof, Generalized Gradient Approximation Made Simple, Phys. Rev. Lett. **77**, 3865 (1996).

[45] J. P. Perdew, A. Ruzsinszky, G. I. Csonka, O. A. Vydrov, G. E. Scuseria, L. A. Constantin, X. Zhou, and K. Burke, Restoring

the Density-Gradient Expansion for Exchange in Solids and Surfaces, Phys. Rev. Lett. **100**, 136406 (2008).

[46] P. E. Blöchl, Projector augmented-wave method, Phys. Rev. B **50**, 17953 (1994).

[47] THERMO_PW, https://dalcorso.github.io/thermo_pw/.

[48] T. Roisnel and J. Rodriguez-Carvajal, Materials Science Forum, in *Proceedings of the Seventh European Powder Diffraction Conference (EPDIC 7)*, edited by R. Delhez and E. J. Mittenmeijer (Trans Tech Publications, Switzerland, 2000), pp. 118–123.

[49] G. Williamson and W. Hall, X-ray line broadening from filed aluminium and wolfram, Acta Metall. **1**, 22 (1953).

[50] G. Courbion and G. Ferey, $Na_2Ca_3Al_2F_14$: A new example of a structure with independent F. A new method of comparison between fluorides and oxides of different formula, J. Solid State Chem. **76**, 426 (1988).

[51] See Supplemental Material at http://link.aps.org/supplemental/10.1103/PhysRevB.103.064109 for additional $\beta(2\theta)$ plots, neutron diffraction patterns at 300 K, other hypothetical structures used in DFT calculations, phonon dispersion relations and electronic band structure calculated with DFT for tetragonal and orthorhombic β-PbO_2 for a broad selection of lines in the reciprocal lattice, and a table with widths of SR diffraction β-PbO_2 peaks observed and calculated using the Stephens model.

[52] R. B. Von Dreele, M. R. Suchomel, and B. H. Toby, Advanced photon source compute x-ray absorption, https://11bm.xray.aps.anl.gov/absorb/absorb.php.

[53] L. B. McCusker, R. B. Von Dreele, D. E. Cox, D. Louër, and P. Scardi, Rietveld refinement guidelines, J. Appl. Crystallogr. **32**, 36 (1999).

[54] J. Gavarri, P. Garnier, P. Boher, A. Dianoux, G. Chedeville, and B. Jacq, Proton motions in battery lead dioxides, J. Solid State Chem. **75**, 251 (1988).

[55] M. Halo, C. Pisani, L. Maschio, S. Casassa, M. Schütz, and D. Usvyat, Electron correlation decides the stability of cubic versus hexagonal boron nitride, Phys. Rev. B **83**, 035117 (2011).

[56] D. Payne, G. Paolicelli, F. Offi, G. Panaccione, P. Lacovig, G. Beamson, A. Fondacaro, G. Monaco, G. Vanko, and R. Egdell, A study of core and valence levels in β-PbO_2 by hard X-ray photoemission, J. Electron Spectrosc. Relat. Phenom. **169**, 26 (2009).

[57] L. Burgio, R. J. H. Clark, and S. Firth, Raman spectroscopy as a means for the identification of plattnerite (PbO_2), of lead pigments and of their degradation products, Analyst **126**, 222 (2001).

[58] Y. N. Zhuravlev and D. V. Korabel'nikov, A first principles study of the mechanical, electronic, and vibrational properties of lead oxide, Phys. Solid State **59**, 2296 (2017).

[59] M. de Jong, W. Chen, T. Angsten, A. Jain, R. Notestine, A. Gamst, M. Sluiter, C. K. Ande, S. van der Zwaag, J. J. Plata, C. Toher, S. Curtarolo, G. Ceder, K. A. Persson, and M. Asta, Charting the complete elastic properties of inorganic crystalline compounds, Sci. Data **2**, 150009 (2015).

[60] F. Bounab, N. Bouarissa, A. Merrouche, A. Benmakhlouf, S. Daoud, and N.-E. Chelali, Theoretical investigation of elastic constants and related properties of compressed PbO_2, J. Comput. Electron. **18**, 1111 (2019).

[61] L. Liu, The high-pressure phase transformations of PbO_2: An in-situ X-ray diffraction study, Phys. Chem. Miner. **6**, 187 (1980).

[62] G. I. Csonka, J. P. Perdew, A. Ruzsinszky, P. H. T. Philipsen, S. Lebègue, J. Paier, O. A. Vydrov, and J. G. Ángyán, Assessing the performance of recent density functionals for bulk solids, Phys. Rev. B **79**, 155107 (2009).

[63] J. Heyd, G. E. Scuseria, and M. Ernzerhof, Hybrid functionals based on a screened Coulomb potential, J. Chem. Phys. **118**, 8207 (2003).

[64] S. Mahatara and B. Kiefer, Does β-PbO_2 harbor topological states? J. Phys.: Condens. Matter **32**, 255504 (2020).